

IMAGE/HENA: Global ENA imaging of the plasma sheet and ring current during substorms

P. C:son Brandt,¹ R. Demajistre,¹ E. C. Roelof,¹ D. G. Mitchell,¹ S. Mende²

Abstract. Energetic neutral atom (ENA) images in the 10-60 keV range of the plasma sheet and ring current region are presented. The images were obtained during two substorms in the mainphase of the 4 October 2000 storm by the high energy energetic neutral atom (HENA) imager onboard the IMAGE satellite. They show ENA emissions extending out into the nightside plasma sheet region of $L \leq 15$. During the two substorm sequences the edge of the most tailward ENA emissions appears to move earthward in association with dipolarization observed at geosynchronous distance by the GOES satellite. At the time of geosynchronous dipolarization, the auroral onset was observed by the far ultra violet (FUV) imager onboard IMAGE. Preliminary equatorial ion distributions derived from the individual ENA images in the substorm sequences have been obtained through a constrained linear inversion technique. The results show that the ion fluxes in the $>6R_E$ plasma sheet suddenly decrease around dipolarization during approximately 30 min. About 10-20 min after the start of the plasma sheet flux decrease, ion injections are seen by the geosynchronous satellites. The peak of the ring current flux is pushed in from geosynchronous to $L=4$ over the substorm sequences. Two exospheric models are used in the inversion. We find that more realistic plasma sheet fluxes are obtained with an exospheric model that contains enhanced exospheric hydrogen densities on the nightside. Implications for Earthward propagation are discussed and an Earthward propagation velocity is estimated to 27-33 km s⁻¹.

1. Introduction

The magnetospheric substorm is still the least understood global magnetospheric phenomena. One of the challenges has been to draw conclusions about the large-scale dynamics from local measurements in the geomagnetic tail and plasma sheet. Many substorm models have been developed, but two main models have emerged. The tail current disruption (TCD) model [Lui, 1991] and the near-Earth neutral line (NENL) model [Baker *et al.*, 1996].

This paper reports the first global images of the energetic ion distributions in the near-Earth plasma sheet out to 15 R_E during two substorms in the mainphase of the 4 October 2000 storm. The images were obtained in the 10-60 keV range with 6 min resolution by the high energy neutral atom

(HENA) imager [Mitchell *et al.*, 2000] onboard the IMAGE satellite [Burch, 2000].

Energetic neutral atoms (ENA) are produced when singly positively charged energetic ions undergo charge-exchange collisions with cold neutral atoms or molecules. The ions become neutral and propagate unaffected by electromagnetic fields. If the initial energy is much greater than the planetary escape energy (0.6 eV/nucleon), then the ENAs are unaffected by gravitational fields and will maintain their energy and momentum. In the terrestrial magnetosphere, the energetic ions will charge exchange with the geocorona at high altitudes and emit ENAs. In this way the ring current and the plasma sheet can be imaged. In addition to carrying with it spectral and directional information of the energetic ions, the ENA also is a direct measurement of the composition of those ions.

The purpose of this paper is to report the first global im-

¹Applied Physics Laboratory, Johns Hopkins University, Laurel, MD

²Space Science Laboratory, Berkeley, CA

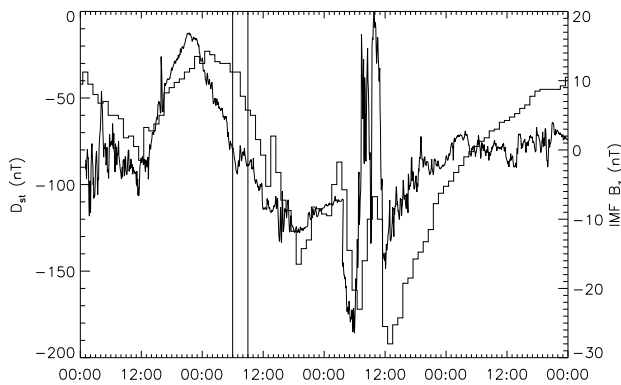


Figure 1. The IMF B_z (bold line) and the D_{st} (thin line) for the 4 October 2000 storm. The two vertical lines mark the time for the two substorms.

ages of the dynamics of the plasma sheet and to present preliminary results of our inversions of the ENA images. The paper first describes the solar wind and geomagnetic conditions during the events. Then the ENA observations are presented together with auroral images from the far-ultraviolet (FUV) imager onboard IMAGE. We then proceed by quantifying the timing of the dynamics in the ENA images. Geosynchronous observations of the magnetic field signatures from GOES and particle injection signatures from the Los Alamos National Laboratory (LANL) satellites are then put in relation to the signatures seen in the ENA images. Last we present and discuss the ion distributions derived from the ENA images through a constrained linear inversion technique. These observations show that the plasma sheet flux drops in association with dipolarization in about 30 min, but are quickly restored in the same time scale.

2. Observations

In this section we will present the ENA images of the substorms, the energetic particle injections and dipolarizations seen at geosynchronous, and the auroral onset seen by IMAGE/FUV.

2.1. Storm conditions

The IMF B_z is plotted together with the D_{st} index in Figure 1. The 4 October 2000 storm displayed an almost 24 hour long mainphase due to a steadily decreasing IMF B_z . The thick line is the IMF- B_z and the thinner is the D_{st} . The two vertical lines at 06:10 UT and 09:22 UT mark the auroral onsets of the two substorms as defined by the far ultra violet (FUV) imager on board IMAGE.

2.2. ENA observations

Plates 1 and 2 show four ENA images during each sub-storm sequence for 10-60 keV and integrated over 6 min (3 spins). The ENA images are presented in an azimuthal equidistant projection with a 180° field of view (FOV). To illustrate the projection one can think of the detector being located in the center of a sphere, with the pole of the sphere being the direction of the spin axis. The image has then been wrapped onto the surface of this sphere and then back projected, with distances preserved, to the image plane tangential to the imagined sphere. The dashed gridlines in the background mark the latitude (horizontal lines) and the longitude (vertical lines) of this sphere. The latitude corresponds to the elevation angle in the instrument and the longitude corresponds to the spin angle. The coordinate system is geocentric. The circle about the center represents the limb of the Earth, while the arc inside the limb represents the terminator. The magnetic dipole field lines of L shells 4, 8 and 12 are drawn for reference at noon, dawn, midnight, and dusk. The magnetic local time (MLT) of each set of field lines is marked in red. All images are taken from a vantage point above the north pole. This projection is closest to what a human eye would see. The weak horizontal bands of emissions at the upper portions of each image (grid longitude -30°) are the solar contamination caused by residual sunlight hitting the detector plates.

During the first sequence of images in Plate 1 we see how the nightside ENA flux increases with time in the $L \leq 4$ region. Note how the ENA emissions from the $L > 8$ region decrease with time. The auroral onset was determined from the IMAGE/FUV images to be at 06:10 UT, corresponding to Plate 1b. The substorm sequence with its onset at 09:22 UT had a clearer ENA signature and is shown in Plate 2. In this sequence it is more evident that the ENA fluxes in the $L > 8$ region decreased significantly after 09:32 UT.

Below we will invert the isotropic component of the equatorial ion distribution from the ENA images in Plates 1 and 2. However, it would require an impractically large number of inversions to accurately time the dynamics. Therefore, we summed the region as marked in Figure 2a and plotted the summed intensities as a function of time. The summed region lies between -30° and $+30^\circ$ map latitude (instrumental elevational angle marked by the horizontal gridlines), and between 60° to 90° map longitude (instrumental spin angle marked by the vertical gridlines).

The minimum L-shell the LOS intersects above 60° spin angle is approximately $L=10$ as is sketched in Figure 2b. This means that the ENAs within the dashed region in Figure 2a were created by ions from $L \geq 10$. These plots are shown for the two different substorms in Figures 3 and 4. In Figure

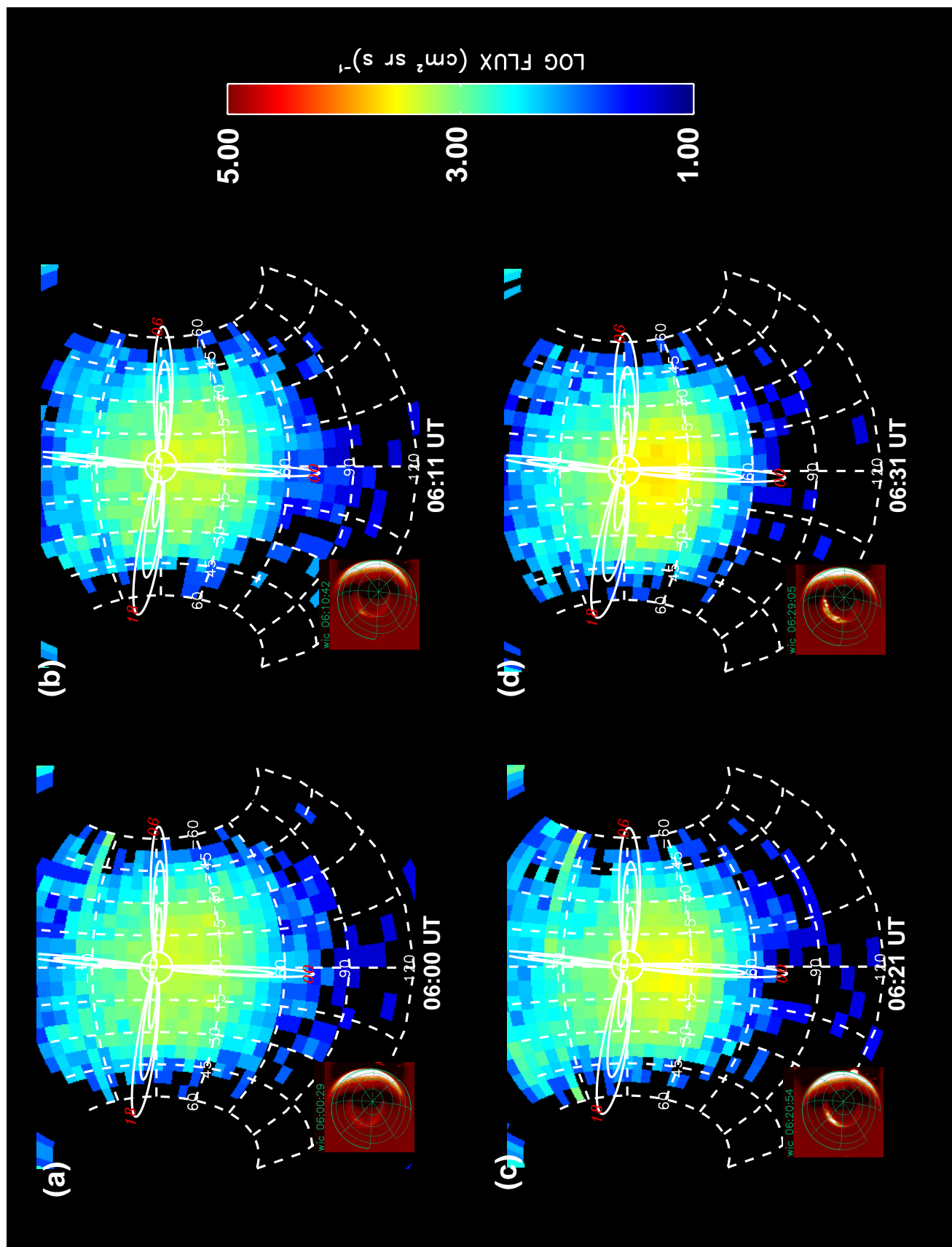


Plate 1. The ENA images in the 10-60 keV range of the first substorm sequence with auroral onset at 06:10 UT. The inset is the auroral image obtained by the FUV/WIC camera on board IMAGE.

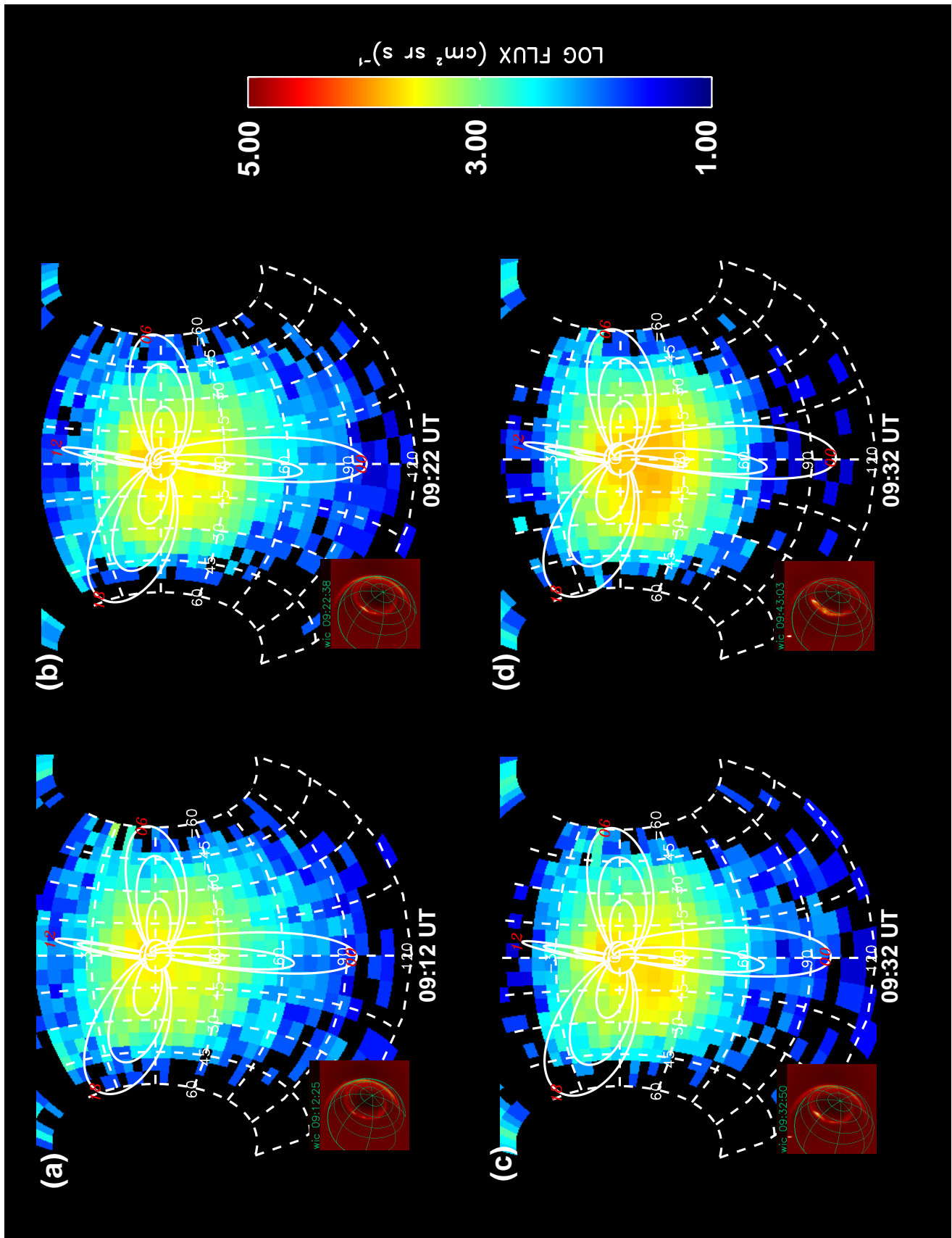


Plate 2. The ENA images in the 10-60 keV range of the second substorm sequence with auroral onset at 09:22 UT. The inset is the auroral image obtained by the FUV/WIC camera on board IMAGE.

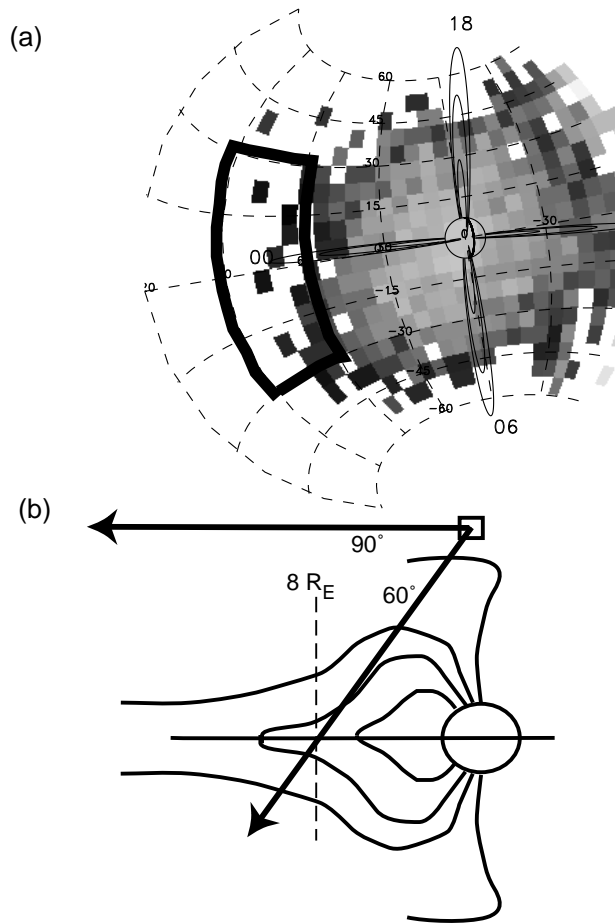


Figure 2. In order to accurately time the dynamics the ENA emissions within the solid line are summed and plotted as a function of time in Figures 3 and 4.

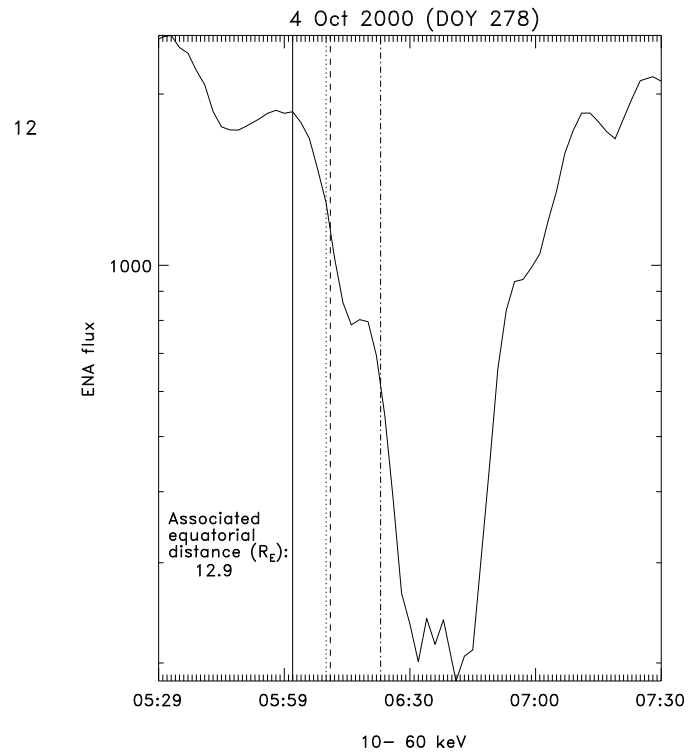


Figure 3. The total ENA intensity as a function of time for the 06:10 UT substorm. The intensity is obtained from the region enclosed by the dashed line in Figure 2.

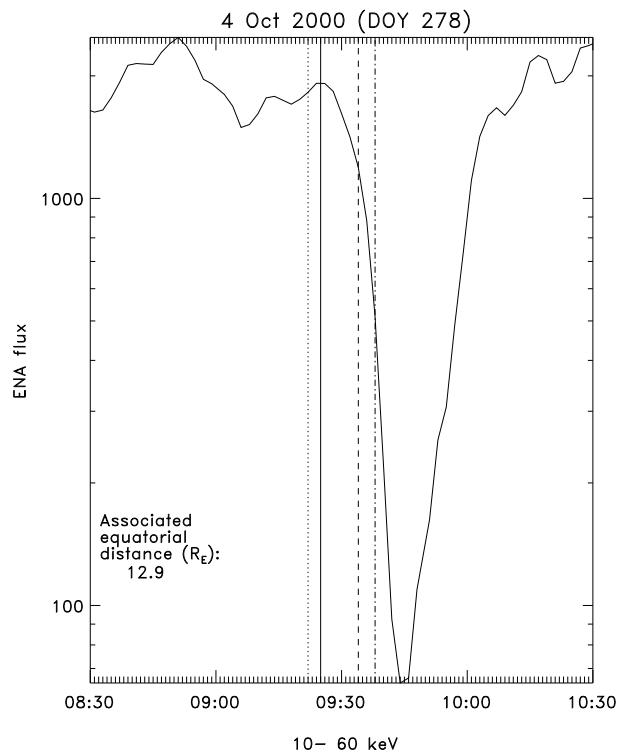


Figure 4. The total ENA intensity as a function of time for the 09:22 UT substorm. The intensity is obtained from the region enclosed by the dashed line in Figure 2.

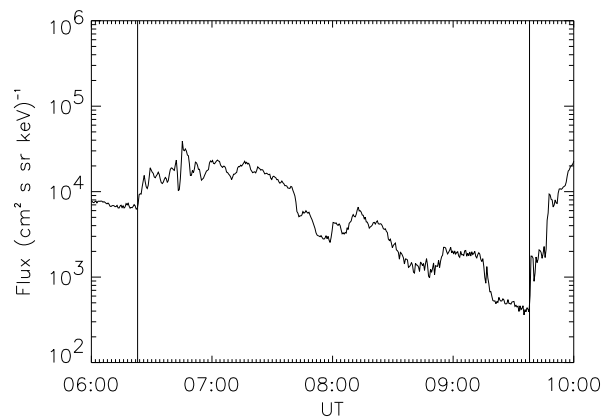


Figure 5. Plot of the 75-113 keV protons at geosynchronous. Vertical lines indicate the injections at 06:23 UT (19:23 MLT) and 09:38 UT (22:38 MLT).

3 we see how the ENA flux from the $L \geq 10$ region starts decreasing rapidly at 06:03 UT ± 2 min. In both Figures 3 and 4 the dotted line marks the auroral onset identified by FUV; the dashed line marks when GOES observed the dipolarization; the dashed-dotted line marks when the particle injection reached the LANL satellite at geosynchronous. There is a corresponding rapid decrease for the $L \geq 10$ ENA fluxes around 09:26 UT ± 2 min as can be seen in Figure 4. Note that the auroral onset was about 4 min before the decrease of the $L \geq 10$ ENA emissions here.

2.3. Geosynchronous ion observations

Figure 5 shows the 75-113 keV protons detected by the LANL satellite 1989-046. The vertical lines mark the injections detected at 06:23 UT (19:23 MLT) and 09:38 UT (22:38 MLT).

Figure 6 shows the geomagnetic B_z (solid) and B_x (dashed) component. The vertical lines mark the dipolarization signature associated with each substorm at 06:11 UT (21:22 MLT) and 09:34 UT (00:47 MLT). The first dipolarization shows very little change in the B_x component which could be due to the fact that the GOES satellite was duskward of the stretched current sheet. At 07:00 UT the B_x component started to increase indicating a more stretched field configuration. At 09:34 UT we see the classical signature of the dipolarization with sharply decreasing B_x and increasing B_z .

2.4. FUV observations

The auroral FUV observations are shown as insets in the lower left corner of Plates 1 and 2. The gridlines represent

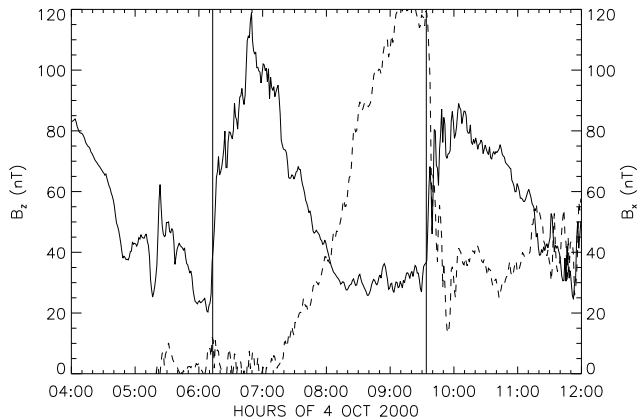


Figure 6. The B_x (dashed) and B_z (solid) component of the geomagnetic field at geosynchronous measured by GOES. The vertical lines mark the dipolarization signatures at 06:11 UT (21:22 MLT) and 09:34 UT (00:47 MLT).

the geomagnetic latitude and longitudes. Latitude gridlines are 10° apart starting at the pole and longitude gridlines are 45° apart. The bright side of the globe is the dayside resulting from resonantly scattered sunlight. Note that the grid appears to change position from image to image. This is due to a wobble of the spacecraft spin axis during this particular date. One should not try to estimate any surface coordinates of the emissions from the grid. We can therefore not determine the magnetic latitude of the onset region. We have determined the two onset times from a high resolution image sequence to 06:10 UT and 09:22 UT.

2.5. Earthward propagation

From the above observations one may estimate a propagation velocity. We do this by taking the time from the start of the decrease at $>10 R_E$ in Figures 3 and 4, until the first ion intensifications are seen at geosynchronous altitude in Figure 5 for the 06:10 and 09:22 UT substorm. This gives us an Earthward propagation velocities of 27 and 33 km s^{-1} for the two substorm injections. These values agree well with in-situ measurements [Huang and Frank, 1994].

3. Inversion method and results

The numerical method we use is called constrained linear inversion and closely follows the method described by Twomey [1977]. However, we utilize two new and, we believe, essential features recently introduced by Roelof [2002] and Demajistre et al. [2002]. First, the unknown variables to be inverted are simply the equatorial ion in-

intensities $j_{ION}(L, \phi, \mu)$ at each discrete location $(L, \phi)_k$ bin in the magnetic equatorial plane. In other words, the output of the inversion method gives the ion distribution itself, rather than coefficients of its expansion in orthogonal functions or numerical splines (e.g., Perez et al. [2001]). Not only does this direct formulation allow an immediate assessment of the physical appropriateness of the result, but it also reproduces more readily phenomenological patterns such as "fronts" and "edges" in the ion distribution whose discontinuities tend to be smoothed by analytical representations. Second, the constraints of the inversion are determined by a novel "tuning" technique based on the ENA image itself. The inversion must be constrained, because it is only weakly over-determined, i.e., the number of pixels in the image is only a small multiple of the number of location bins $(L, \phi)_k$ needed to describe the ion distribution.

The number of counts accumulated in the i th camera pixel is written in terms of the averaged normal area $\langle A_i(\epsilon, \beta) \rangle$ of the camera seen by an ENA incident on the instrument from elevation angle ϵ and azimuth angle β .

$$C_i = \Delta t \int d\epsilon \sin\epsilon \int d\beta \langle A_i(\epsilon, \beta) \rangle J_{ENA}(\epsilon, \beta) \quad (1)$$

We write $J_{ENA}(\epsilon, \beta)$ for $j_{ENA}(\epsilon, \beta)\Delta E$ because we assume that the energy (or velocity) pass bands ΔE are narrow enough so that there is no significant variation in the camera response. The integral over the angles (ϵ, β) in principle covers the entire sky (4π sr) and not just the small solid angle of a single pixel. This is because each pixel has a "point-spread" function owing to internal scattering that can be significantly larger than the pixel itself. The averaging of A_i is over the time Δt during which the counts are accumulated in the pixel, e.g., a minimum of one spin ($\Delta t=120$ s) for IMAGE/HENA. It also must be integrated over the solid angle of the pixel and any significant orbital motion of the spacecraft during the exposure time for the pixel. All properties of the ENA camera must be incorporated into the function $\langle A_i(\epsilon, \beta) \rangle$. Examples for other ENA instruments have been published: the MEPI particle telescope on ISEE-1 [Roelof, 1987] and the PIPPI camera on Astrid-1 [C:son Brandt et al., 2001]. The detailed description for HENA is given by Roelof [2002].

The well-known relationship between the differential number flux j_{ENA} and j_{ION} for an "ENA optically thin" medium is expressed in terms of a line-of-sight (LOS) integral. The simplest case is that of "high-altitude" ENA imaging of ring current ions immersed in the hydrogen geocorona

$$j_{ENA} = \sigma_H^{1,0}(E) \int ds n_H(r) j_{ION}^{eq}(L, \phi, \mu_{eq}), \quad (2)$$

where \mathbf{s} is the distance vector from the point of emission \mathbf{r} the camera at position \mathbf{R} along the LOS. Thus $\mathbf{s} = \mathbf{R} - \mathbf{r}$

gives the direction of the ENA. The cross section for charge exchange is $\sigma_H^{1,0}(E)$, and $n_H(r)$ is the geocoronal hydrogen density. We assume that there is negligibly weak scattering of the ion along the magnetic field line. Then the magnetic moment $(1 - \mu^2)/B$ is conserved and the ion intensity j_{ion} with pitch-cosine μ at any point on a field line may be related via Liouville's theorem to j_{ION}^{eq} with pitch-cosine μ_{eq} at that lines' equatorial crossing. Again, we shall assume energy resolution good enough that j_{ENA} and j_{ION}^{eq} may be replaced by $J_{ENA} = j_{ENA} \Delta E$ and $J_{ION}^{eq} = j_{ION}^{eq} \Delta E$.

Now Equations 1 and 2 may be combined. Usually, the integrations are carried out as indicated, first along the LOS and then over the angular response of the instrument. However *Roelof* [2002] has noted that the triple integral over the instrument arrival solid angle and LOS can be transformed into a volume integral in geomagnetic spherical polar coordinates. The exact Jacobian is r^2/s^2 , so we have

$$d\epsilon \sin \epsilon d\beta ds = dr d\theta \sin \theta d\phi \frac{r^2}{s^2}, \quad (3)$$

where θ is the geomagnetic co-latitude and ϕ is the magnetic longitude (MLT). If we furthermore approximate the geomagnetic field by a dipole, then $dr = (\arcsin^2 \theta) dL$ when the innermost integral over volume is taken over θ . Obviously, $a = 1R_E$. The final result is

$$C_i = \int dL \int d\phi K_i(L, \phi) J_{ION}^{eq}(L, \phi, \mu_{eq}), \quad (4)$$

where

$$K_i(L, \phi) = a \sigma_H^{1,0} \Delta t \int d\theta \sin^3 \theta \frac{r^2}{s} n_H(r) \langle A_i(\epsilon, \beta) \rangle \quad (5)$$

In passing from Equation 4 to 5 we have neglected the pitch-angle dependence in $J_{ION}^{eq}(L, \phi, \mu_{eq})$, i.e., we have made the approximation of an isotropic equatorial ion distribution. This will be adequate for this paper, which only deals with ENA images taken at high latitudes during periods when pitch-angle effects appear to be negligible. The more general case is treated by *Roelof* [2002].

The integral over colatitude θ for the kernel in Equation 5 is carried out (using an efficient integration algorithm) for each equatorial position bin $(L, \phi)_k$. Then the double integral in Equation 4 can be approximated by linear quadratures.

$$C_i = \sum_k K_i(L, \phi)_k J_{ION}^{eq}(L, \phi)_k, \quad (6)$$

where the index k runs over all equatorial position bins (L, ϕ) . We have thus achieved our goal of formulating an ENA image inversion explicitly in terms of the equatorial ion intensities indexed by their position bins $(L, \phi)_k$.

In more concise matrix/vector notation we write $\mathbf{C} = \mathbf{K}\mathbf{J}$, where \mathbf{K} is a non-square matrix because there are more pixels (i) than position bins (k). The elements in \mathbf{K} are not exactly $K_i(L, \phi)_k$, but rather are linear combinations thereof resulting from the particular quadrature formula applied to Equation 4. The constrained least-squares solution for this linear system is [*Twomey*, 1977]

$$\mathbf{J} = (\mathbf{K}\mathbf{T}\mathbf{K} + \gamma\mathbf{H})^{-1} \mathbf{K}^T \sigma^{-2} \mathbf{C} \quad (7)$$

where σ^{-2} is the inverse of the covariance matrix of the pixel counts, \mathbf{H} is a smoothing matrix, and γ is the constraint strength.

Now we come to the second innovation, the "tuning" of the constraint strength. The "regularization" $\gamma\mathbf{H}$ must be large enough to stabilize the inversion, but small enough to avoid unnecessary distortion. In nearly all cases that we have tested, the unconstrained inversion ($\gamma=0$) is very poorly conditioned. In order to "tune" the regularization, we first simulate an ENA image using Equation 4 with the 38-parameter model developed by *Roelof and Skinner* [2000]. We choose the parameters to produce a test ion distribution $J_k^{(0)}$ that we estimate should produce an ENA image similar to the one we are trying to invert. This could be thought of as a first guess at the result. We add Poisson counting statistics to the counts $C_i^{(0)}$ in the simulated ENA image. We then invert the image using Equation 7 and our first guess at the value of the constraint strength $\gamma^{(0)}$. This gives us a solution $J_k^{(1)}$ that we compare with $J_k^{(0)}$. This comparison tells us if $\gamma^{(0)}$ was too small (inversion ill-conditioned) or too large (solution overly smoothed), leading us to our next guess $\gamma^{(1)}$. We can also adjust the form of \mathbf{H} at each step. We have tried several forms of \mathbf{H} and have found that the minimum length solution ($\mathbf{H} = \mathbf{I}$, the identity matrix) consistently exhibits the most stable behavior. We repeat this process n times until we find a suitable combination of $\gamma^{(n)}$ and $\mathbf{H}^{(n)}$, i.e., one such that $\mathbf{J}_k^{(n)}$ reproduces the essential spatial features of the test distribution $\mathbf{J}_k^{(0)}$. Finally, we obtain our actual solution by using $\gamma^{(n)}$ and $\mathbf{H}^{(n)}$ in Equation 7 to invert the observed pixel counts C_i for our best estimate of the equatorial ion intensities $J(L, \phi)_k$.

In brief, what we have done is to iteratively "tune" the regularization so that it faithfully retrieves a test ion distribution that can simulate an ENA image that looks like the observed ENA image. If the test intensity function is similar to the actual ion intensity that we finally invert from the ENA image, then our process is self-consistent. This "tuning" process is greatly facilitated by formulating the inversion problem directly in terms of the equatorial ion intensity distribution $J_{ION}^{eq}(L, \phi, \mu_{eq})$ as specified in Equation 4.

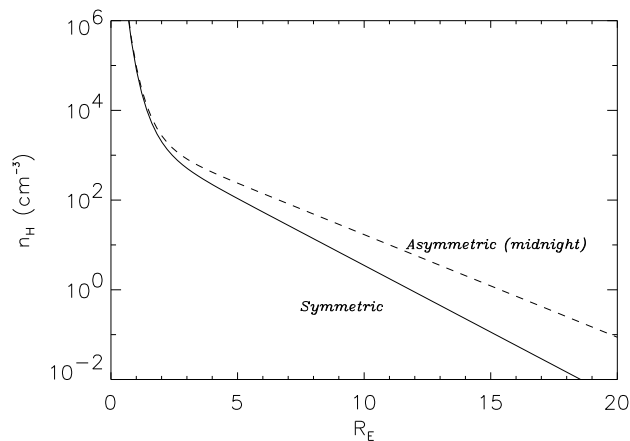


Figure 7. The two exospheric models used. The dashed line display enhanced exospheric densities at large altitudes on the nightside.

4. Exosphere

To illustrate the effects of the exosphere we use here the symmetric Chamberlain model [Chamberlain, 1963] and an asymmetric model based on the DE-1 measurements reported by Rairden *et al.* [1986]. They provided measured column densities of the nightside exosphere which showed an excess over the symmetric Chamberlain model which often is referred to as a “geotail”. Both models can be described by

$$n(R, \phi) = 3300 \exp\left[17.5e^{-1.5R} - \frac{R}{H(\phi)}\right], \quad (8)$$

where

$$H(\phi) = 1.46[1 - k \sin(\theta) \cos(\phi)]. \quad (9)$$

Here ϕ is the local time angle from noon and θ is the polar angle from the z-axis in the Geocentric Solar Magnetic (GSM) coordinate system. A non zero value of k allows one to represent the geotail in the form of an axis-symmetric (around the sun-earth line) exosphere. Setting $k = 0$ restores the symmetric Chamberlain model. All numeric coefficients in the above expressions have been obtained from the fit to the Chamberlain model by Rairden *et al.* [1986]. By fitting their column densities of the geotail to Equations 8 and 9 we obtain $k = 0.3$. The symmetric and axis-symmetric model is plotted for $\phi=180^\circ$ in Figure 7. We would like to stress that although the existence of a geotail is confirmed, the quantitative knowledge is thin.

5. Results

The ENA images in Plates 1 and 2 have been inverted using the two exospheric models above ($k=0$ and $k=0.3$ in Equation 9).

The inversions of the ENA image sequence in Plate 1 are shown in Plates 3 with the symmetric exosphere and in Plate 4 with the asymmetric exosphere. The ion distribution is plotted in L-MLT coordinates out to $L=15$. In fact, the ion flux in the inversion is clamped to zero at $L < 2$ and $L > 15$.

The effects from the contamination of residual sunlight in the detector is clearly visible on the dayside at $L \lesssim 6$ as the enhanced intensities. We have chosen to show the contamination in this paper to illustrate how and when it effects the data, and more important, how to eliminate it from the ion distribution. The LOSs toward the sun contamination in Plates 1 and 2 (above map grid longitude -30°) intersects a minimum L-shell of 6 for both substorms and therefore ion distributions below $L=6$ are free of solar contamination. Also, the field of view (FOV) of the instrument cuts off the edges outside $|45^\circ|$ instrumental latitude. Here the sensitivity of the instrument is low and thus the response function amplifies the uncertainties. Therefore we stress that the empty regions on the dusk and dawn sides in the inverted results below are the effects of the finite FOV of the instrument and not zero flux.

At 06:01 UT (Plate 3a) the ion distribution display large fluxes out to $13 R_E$ in the post midnight sector with its peak at $6 R_E$. The enhancement around $6 R_E$ extends from post midnight to the dusk sector. In the remaining sequence (Plates 3b-3d) the nightside fluxes above $7 R_E$ decreases. The peak of the ion distribution moves earthward from about $6 R_E$ to $5 R_E$ and spreads also in local time.

Plate 4 shows the sequence of inversions using the asymmetric exospheric model with $k = 0.3$. It is immediately clear that the ion fluxes are in general weaker than for the inversions in Plate 3 with $k = 0$. The reason for this is that the asymmetric exosphere displays higher density than the symmetric model does, as can be seen in Figure 7 and so less ion flux is required to match the observed ENA images. At 06:01 UT there are relatively high ion fluxes out to $13 R_E$, which move gradually earthward throughout Plates 4b-4d. We can see that the peak ion flux moves from $6 R_E$ to about $4 R_E$ and expand also in local time. A similar development can be seen for the 09:22 UT substorm shown in Plates 5 and 6. The corresponding ENA images are shown in Plate 2. Plate 5 shows the inversion using the symmetric model exosphere with $k=0$. The overall fluxes are slightly higher than for Plate 3 and appears to be more confined in MLT. Again, we see intense ion fluxes out to $13 R_E$ that decreases throughout the sequence that may be interpreted as an Earth-

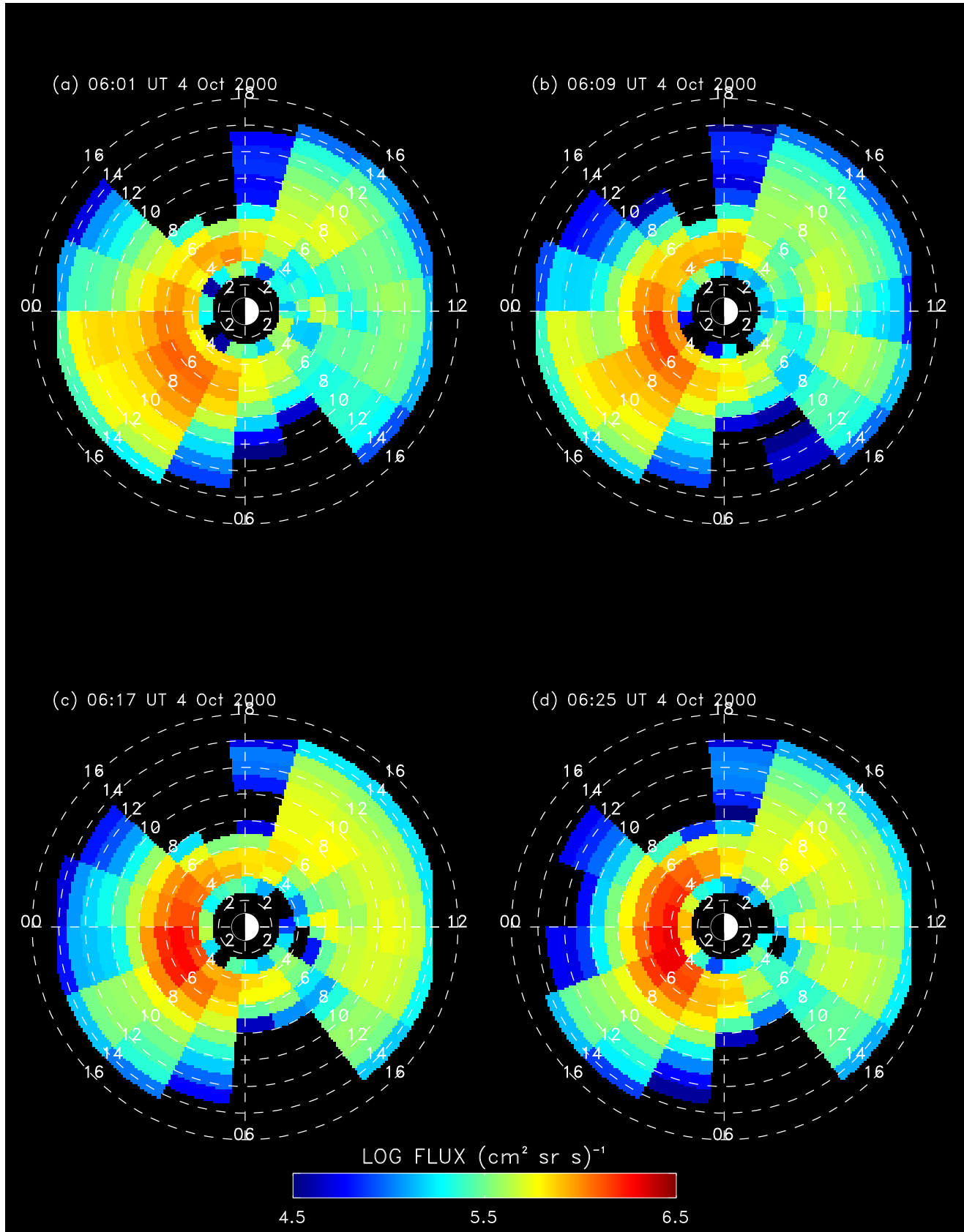


Plate 3. The inverted ion distributions in the 10-60 keV range (6 min integration) for the 06:11 UT substorm using the symmetric *Rairden et al.* [1986] model exosphere (see Equations 8 and 9).

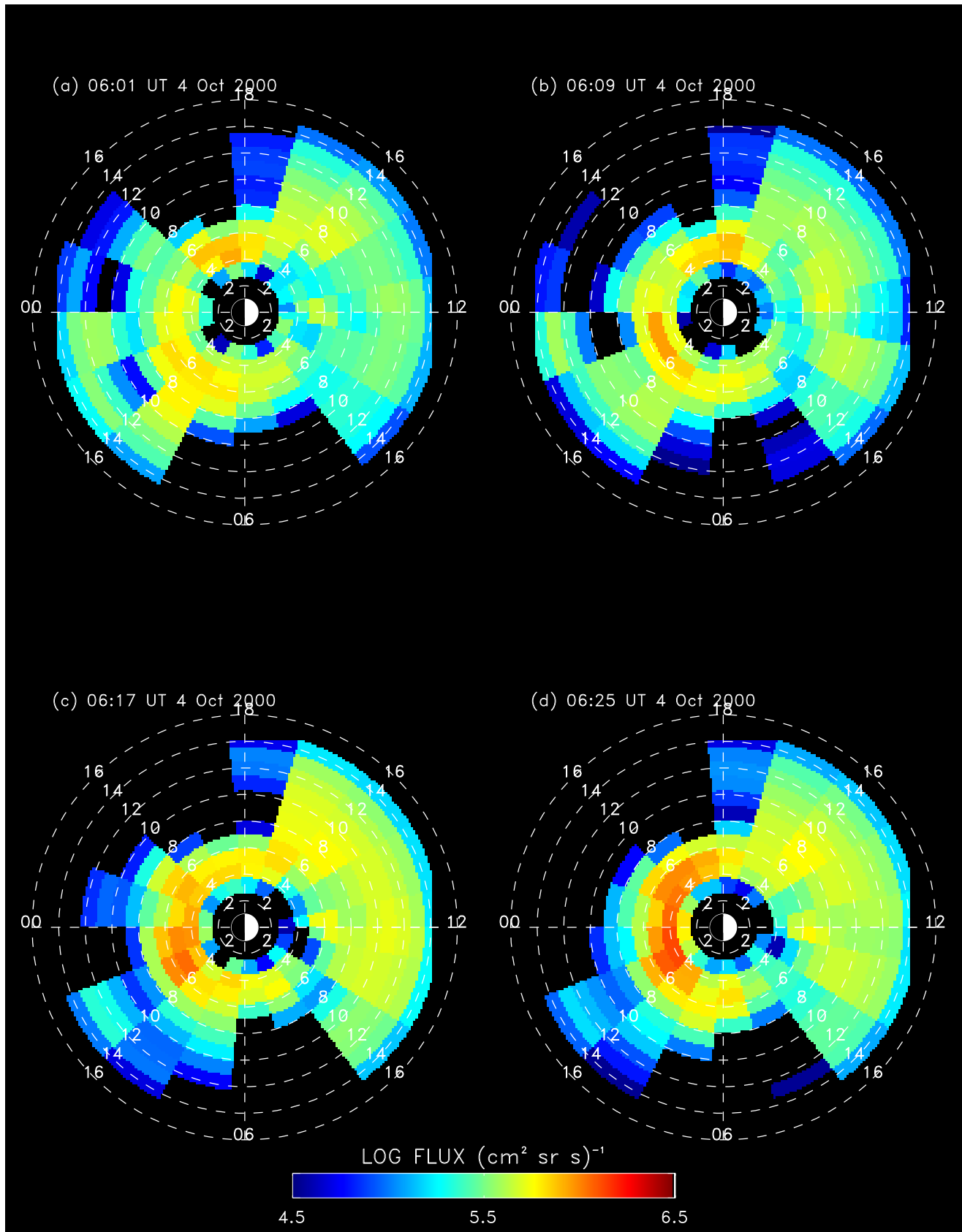


Plate 4. The inverted ion distributions in the 10-60 keV range (6 min integration) for the 06:11 UT substorm using the asymmetric *Rairden et al. [1986]* model exosphere with $k = 0.3$ from Equations 8 and 9.

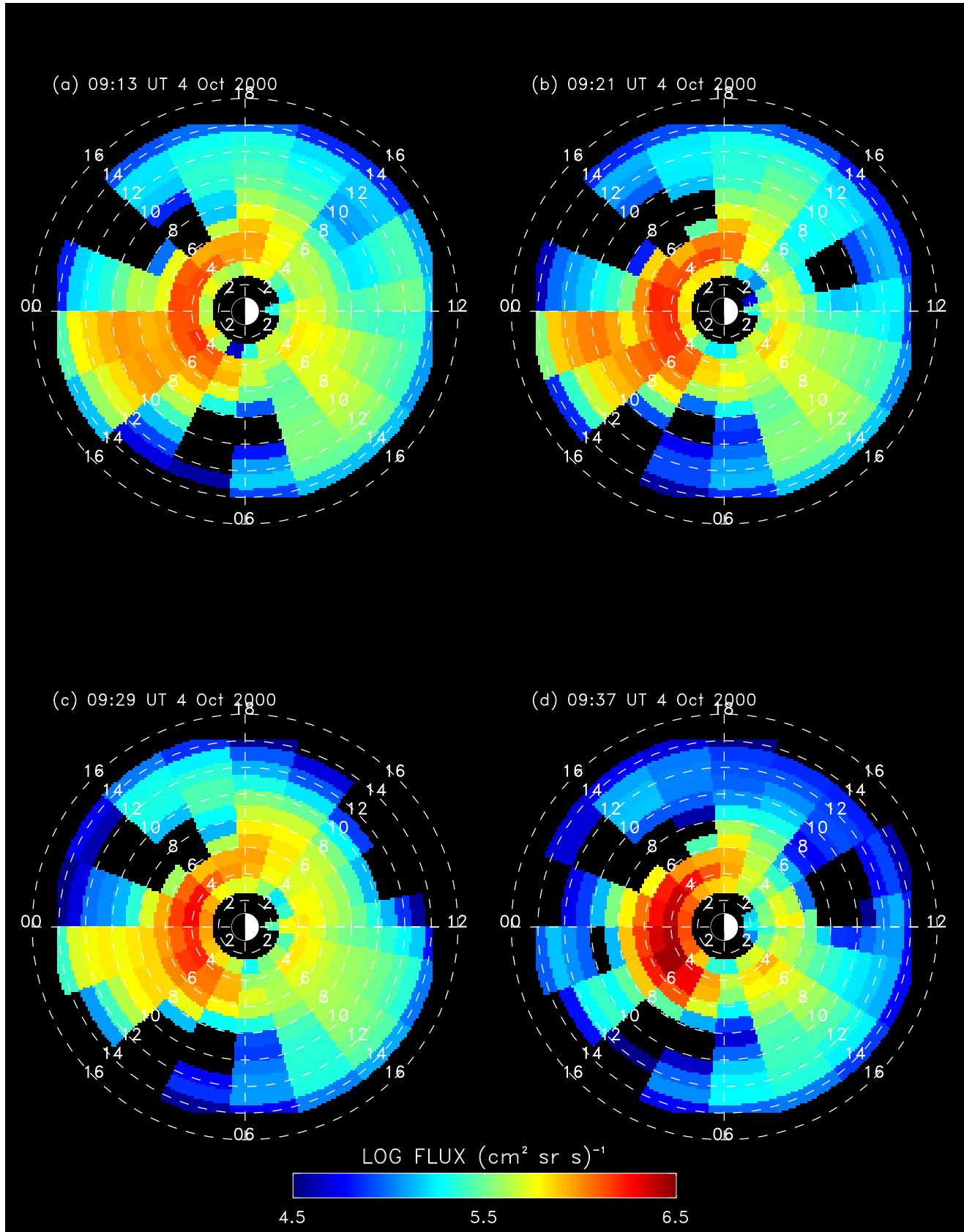


Plate 5. The inverted ion distributions in the 10-60 keV range (6 min integration) for the 09:22 UT substorm using the *Rairden et al.* [1986] model exosphere (see Equations 8 and 9).

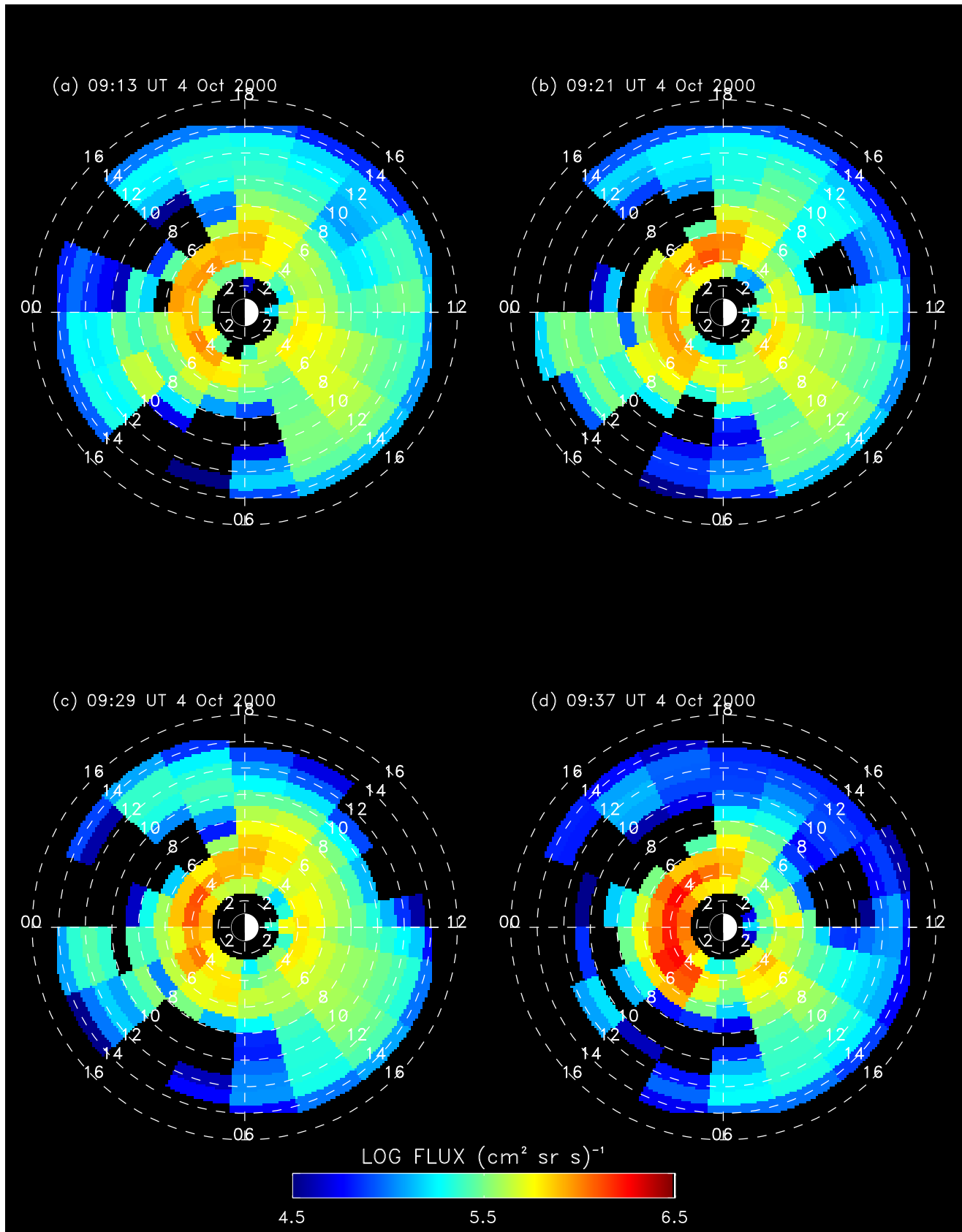


Plate 6. The inverted ion distributions in the 10-60 keV range (6 min integration) for the 09:22 UT substorm using the asymmetric *Rairden et al. [1986]* model exosphere with $k = 0.3$ from Equations 8 and 9.

ward motion. The peak ion flux moves from $5 R_E$ to $4 R_E$ as it also increases due to the substorm injection. In Plate 5a a minimum appears to develop in the 2230-0130 MLT wedge at around $7 R_E$. One may be tempted also to attribute a tailward propagation of this minimum, or the maximum beyond it. Although interesting we must caution the reader that this could be an effect of our use of a pure dipole field in the inversion. Any findings concerning this feature will be reported in a future paper.

Plate 6 shows the inversion using the asymmetric model exosphere with $k = 0.3$. Again, the overall fluxes are lower than the symmetric model.

6. Discussion

It is worthwhile attempting to put our observations in a physical context. Here we outline a plausible scenario. Before substorm onset at 06:10 UT the cross tail electric field appears to be enhanced due to a negative or very small positive IMF B_z . This enhances the convection from the dayside magnetopause and the Earthward $\mathbf{E} \times \mathbf{B}$ drift on the nightside, resulting in a tail and a plasma sheet with higher ion flux than normal. This appears as the higher ion flux above geosynchronous altitude in Plate 3. The IMF B_z steadily decreases and therefore the cross tail current will build up until it disrupts at some place due to some internal instability [Lui, 1991] or triggering from the NENL [Baker et al., 1996; Ohtani, 2001; Slavin et al., 2001]. The disruption causes the stretched magnetic field configuration to dipolarize which induces an intense dawn-to-dusk electric field pulse. The dipolarization is observed at geosynchronous by GOES around 06:11 UT as shown in Figure 6. At this time the ion fluxes at geosynchronous have increased slightly. The reason for the rapidly decreasing plasma sheet flux accompanying the dipolarization, is that the induced dawn-to-dusk electric field will transport the ions earthward through enhanced $\mathbf{E} \times \mathbf{B}$ drift, faster than the particles can be replenished by the overall $\mathbf{E} \times \mathbf{B}$ drift set up by the convective electric field. The ions have now reached lower altitudes and have been energized through betatron and possibly fermi acceleration. This is where they are observed by the LANL satellite in Figure 5.

Now, since the IMF B_z is still decreasing to more negative values, a steady supply of plasma is convected in from the dayside over the poles on reconnected field lines and will increase the nightside ion flux as soon as the first dipolarization and the substorm injection is complete. The plasma sheet will thin, the cross tail current will build up and the process will repeat itself for the next substorm. This pattern repeated itself several times during the entire day of 4 October.

From our observations it appears that the particle pressure increased in the $>6 R_E$ plasma sheet steadily before dipolarization. At dipolarization the pressure outside $8 R_E$ decreased rapidly while the pressure inside $8 R_E$ increased. Kistler et al. [1992] found that the pressure increased at distances $<10 R_E$ and either decreased or stayed the same outside $10 R_E$. We feel that it may be dangerous to generalize the pressure profiles of substorms without studying the IMF. The reason is that an enhanced external cross tail electric field enhances the Earthward $\mathbf{E} \times \mathbf{B}$ drift and therefore increases the particle pressure through adiabatic energization. However, the loading of fresh solar wind plasma from the lobes would act to decrease the temperature of the plasma sheet and therefore act as a competing process to cool the plasma sheet. This balance between these processes are clearly dependent on IMF and a deeper study of their effect is beyond the scope of this paper. Several facts imply that the ions do undergo an Earthward propagation: (1) After plasma sheet fluxes decrease, the fluxes around geosynchronous increase; (2) Several studies of in-situ measurements have shown that earthward flow occurs mainly within $30 R_E$ [Ohtani, 2001].

7. Summary and conclusions

We have presented the first global images and ion distributions of the Terrestrial plasma sheet out to $14 R_E$. The images were obtained by the HENA instrument on board IMAGE during two substorms in the mainphase of the 4 October, 2001, storm. A constrained linear inversion method was used to derive the ion distribution from the ENA images. The inversion uses a dipole magnetic field and an exospheric model based on the DE-1 observations reported by Rairden et al. [1986]. We summarize our findings as follows.

1. Before the substorm the ion fluxes above geosynchronous were high due to an enhanced convection in the storm mainphase.
2. Ion fluxes above $10 R_E$ started to decrease 8 min before geosynchronous dipolarization (GOES) and 13-16 min before geosynchronous injection (LANL). If this is interpreted as an Earthward propagation the estimated flow velocities are in the range $27\text{-}33 \text{ km s}^{-1}$.
3. Plasma sheet fluxes decrease one order of magnitude after the dipolarization. After the substorm the fluxes are restored. We interpret the decrease in plasma sheet flux as the plasma sheet ions being accelerated earthward by the induced substorm electric fields, faster than they can be replenished from the overall convection. After the substorm, plasma sheet fluxes increase due to the refilling from the convection.

4. The use of a symmetric exospheric model based on the fit by Rairden *et al.* [1986] gave peak plasma sheet fluxes at $L=10$ about $5 \cdot 10^5 (\text{cm sr s})^{-1}$, while an asymmetric exosphere, with a nightside excess of neutral densities, gave about a factor of five lower plasma sheet flux.

We would like to stress that the inversion results reported here are preliminary and qualitative results. The inversion method still needs refinement, such as more accurately incorporating the production mechanism for the ENAs originating from the interaction between the ions and the exobase. A more quantitative study of the storm-substorm relationship during the 4 October storm will be published soon.

Acknowledgments.

References

- Baker, D. N., T. I. Pulkkinen, V. Angelopoulos, W. Baumjohann, and R. L. McPherron, Neutral line model of substorms: Past results and present view, *J. Geophys. Res.*, , *101*, 12,975–13,010, 1996.
- Burch, J. L., ed., *The IMAGE mission*, Kluwer Academic, 2000, reprinted from *Space Sci. Rev.*, vol. 91, Nos. 1-2, 2000.
- Chamberlain, J. W., Planetary coronae and atmospheric evaporation, *Planetary and Space Sci.*, pp. 901–960, 1963.
- C:son Brandt, P., S. Barabash, E. C. Roelof, and C. J. Chase, ENA imaging at low altitudes from the Swedish microsatellite Astrid: Extraction of the equatorial ion distribution, *J. Geophys. Res.*, *106*, 25,731–25,744, 2001.
- Demajistre, R., E. C. Roelof, P. C:son Brandt, and D. G. Mitchell, Retrieval of global magnetospheric ion distributions from high energy neutral atom (ena) measurements by the image/hena instrument, *J. Geophys. Res.*, , 2002, to be submitted.
- Huang, C. Y., and L. A. Frank, A statistical survey of the central plasma sheet, *J. Geophys. Res.*, , *99*, 83–95, 1994.
- Kistler, L. M., E. Möbius, W. Baumjohann, G. Paschmann, and D. C. Hamilton, Pressure changes in the plasma sheet during substorm injections, *J. Geophys. Res.*, , *97*, 2973–2983, 1992.
- Lui, A. T. Y., A synthesis of magnetospheric substorm models, *J. Geophys. Res.*, *96*, 1849–1856, 1991.
- Mitchell, D. G., et al., High energy neutral atom (HENA) imager for the IMAGE mission, *Space Sci. Rev.*, *91*, 67–112, 2000.
- Ohtani, S.-I., Substorm trigger processes in the magnetotail: Recent observations and outstanding issues, *Space Sci. Rev.*, *95*, 347–359, 2001.
- Perez, J. D., G. Kozłowski, P. C. Brandt, D. G. Mitchell, J. M. Jahn, C. J. Pollock, and X. Zhang, Initial ion equatorial pitch angle distributions from energetic neutral atom images obtained by IMAGE, *Geophys. Res. Lett.*, *28*, 1155–1158, 2001.
- Rairden, R. L., L. A. Frank, and J. D. Craven, Geocoronal imaging with dynamics explorer, *J. Geophys. Res.*, *91*, 13,613–13,630, 1986.
- Roelof, E. C., Energetic neutral atom image of a storm-time ring current, *Geophys. Res. Lett.*, *14*, 652–655, 1987.
- Roelof, E. C., Low-altitude ena emissions, *J. Geophys. Res.*, , 2002, to be submitted.
- Roelof, E. C., and A. J. Skinner, Extraction of ion distributions from magnetospheric ENA and EUV images, *Space Sci. Rev.*, *91*, 437–459, 2000.
- Slavin, J. A., et al., Simultaneous observations of earthward flow bursts and plasmoid ejection during magnetospheric substorms, *J. Geophys. Res.*, , 2001, in press.
- Twomey, S., *Introduction to the mathematics in remote sensing and indirect measurements*, Developments in geomathematics 3, 1st ed., Elsevier scientific publishing company, 1977.
- Pontus C:son Brandt, Applied Physics Laboratory, Johns Hopkins University, Laurel, MD

This preprint was prepared with AGU's L^AT_EX macros v4, with the extension package 'AGU++' by P. W. Daly, version 1.5f from 1998/07/16.